Robust Scheduling of Integrated Electricity-heat-hydrogen System Considering Bidirectional Heat Exchange Between Alkaline Electrolyzers and District Heating Networks

Pengfei Han, Xiaoyuan Xu, Zheng Yan, Mohammad Shahidehpour, *Life Fellow*, *IEEE*, Zhenfei Tan, Han Wang, and Gang Li

***Abstract*—The integrated electricity-heat-hydrogen system (IEHHS) facilitates the efficient utilization of multiple energy sources, while the operational flexibility of IEHHS is hindered by the high heat inertia of alkaline electrolyzers (AELs) and the variations of renewable energy. In this paper, we propose a robust scheduling of IEHHS considering the bidirectional heat exchange (BHE) between AELs and district heating networks (DHNs). First, we propose an IEHHS model to coordinate the operations of AELs, active distribution networks (ADNs), and DHNs. In particular, we propose a BHE that not only enables the waste heat recovery for district heating but also accelerates the thermal dynamics in AELs. Then, we formulate a two-stage robust optimization (RO) problem for the IEHHS operation to consider the variability of renewable energy in ADNs. We propose a new solution method, i. e., multi-affine decision rule (MADR), to solve the two-stage RO problem with less conservatism. The simulation results show that the operational flexibility of IEHHS with BHE is remarkably improved compared with that only with unidirectional heat exchange (UHE). Compared with the traditional affine decision rule (ADR), the MADR effectively reduces the IEHHS operating costs while guaranteeing the reliability of scheduling strategies.**

***Index Terms*—Alkaline electrolyzer (AEL), active distribution network (ADN), district heating network (DHN), integrated electricity-heat-hydrogen system (IEHHS), multi-affine decision rule (MADR), robust optimization (RO).**

Manuscript received: August 5, 2024; revised: September 27, 2024; accepted: November 20, 2024. Date of CrossCheck: November 20, 2024. Date of online publication: January 23, 2025.

This work was supported by the Science and Technology Project of State Grid "Research and Application of Wide Area Multi energy Storage Collaborative Optimization and Control Technology in Provincial Power Grid".

P. Han, X. Xu, Z. Yan (corresponding author), Z. Tan, and H. Wang are with the Key Laboratory of Control of Power Transmission and Conversion, Ministry of Education, and Shanghai Non-carbon Energy Conversion and Utilization Institute, Shanghai Jiao Tong University, Shanghai 200240, China (e-mail: han_pf@sjtu.edu.cn; xuxiaoyuan@sjtu.edu.cn; yanz@sjtu.edu.cn; zftan@outlook.com; wanghan9894@sjtu.edu.cn).

M. Shahidehpour is with Electrical and Computer Engineering, Illinois Institute of Technology, Chicago, USA (e-mail: ms@iit.edu).

G. Li is with State Grid Anhui Electric Power Co., Ltd., Hefei 230022, China (e-mail: gl_155@126.com).

DOI: 10.35833/MPCE.2024.000810

I. Introduction

WITH the increasing proliferation of renewable energy generation (REG), the full accommodation of REG within electric power systems becomes more challenging. In this context, the hydrogen production from water electrolysis has been a promising way to reduce REG curtailments and will play a crucial role in constructing a carbon-free energy system. Hence, it is worthwhile to explore efficient cooperation methods for existing hydrogen and energy systems.

It has been pointed out in [1]-[4] that the hydrogen production from solar energy and electricity during valley periods is profitable. In [5], a predictive control method is proposed to balance the REG supply and hydrogen production in an integrated electricity and hydrogen system, where the excessive switching of electrolyzers is circumvented. Owing to the suitable ramping rate and overloading capability of electrolyzers, the hydrogen production systems have been utilized as energy storage units to participate in power system operations [6], [7]. Meanwhile, due to the safety issue of hydrogen-to-oxygen (HTO) conversion, it is essential to include the electrolyzer operation constraints in the coordinated hydrogen production and power system operations [8]. Reference [9] considers the production, standby, and off states in establishing the operation strategies of alkaline electrolyzers (AELs) under volatile electricity prices. Reference [10] models the transitions among AEL states to consider the uncertainty of REG in hydrogen production.

Furthermore, the waste heat recovery from AELs for district heating has drawn wide attention [11], [12]. Hence, it is of great value to explore the operation strategies of integrated electricity-heat-hydrogen systems (IEHHSs) for coordinating the supply of electric and heat demands and the hydrogen production. Reference [11] investigates the optimal scheduling of renewable energy for hydrogen and heat conversion. The cost of heating is reduced by utilizing the exhaust heat from AEL cooling circuits. Reference [12] analyzes the effectiveness of combined heat and hydrogen production using electricity. To utilize the variable REG for hydrogen production and district heating, [13] establishes the IEHHS model considering the operational efficiency of AELs.

Reference [14] develops a receding optimization model to unleash the cross-sectoral operational flexibility and reduce the operating costs of IEHHSs.

In the aforementioned studies, the transition time between AEL states is assumed to be constant and prolonged due to the high thermal inertia of AELs, which would limit the operational flexibility of AEL and thus affect the IEHHS efficiency. Considering the heat exchanges between AELs and heating networks, the district heating networks (DHNs) could be used to accelerate the thermal dynamics and shorten the transition time between AEL states, which is often overlooked in the existing literature.

Another critical issue in the IEHHS operation is to consider the uncertainties associated with REG. Stochastic programming (SP), robust optimization (RO), and distributionally robust optimization (DRO) methods are commonly used to optimize the operation of hydrogen-based multi-energy system under uncertainty. In [15], the IEHHS operation with variable REG is established as an SP problem. In [16], a multi-stage SP method is developed to deal with the long-term uncertain market tendency and short-term uncertain power of REG. This SP method performs well in terms of economy but ignores the feasibility of excluded scenarios.

The RO methods guarantee the feasibility of schedules even in the extreme scenarios but might offer conservative results in the worst-case scenarios. To reduce the conservatism of traditional RO methods, the adjustable RO method is adopted in [17] and [18] for the operation of integrated electricity-heat system. Here, the unit commitment and economic dispatch are conducted at the first stage based on the day-ahead predictions of REG, and the variables are properly adjusted at the recourse stage according to the realization of uncertain REG. The DRO method has also been developed to remedy the deficiencies of RO methods by optimizing the SP solutions under the worst-case probability distributions rather than the robust solution in the worst-case scenarios [19], [20]. Meanwhile, the DRO method utilizes an ambiguity set of probability distributions to model uncertain factors, which increases the complexity and scales of optimization problems.

The solution methods, including the column-and-constraint generation [17], dynamic programming [21], and the affine decision rule (ADR) [18], [22], are widely utilized in the existing literature. Compared with other solution methods, ADR offers real-time scheduling strategies for adjustable variables by mapping them as affine functions of uncertain factors. However, the corresponding operating cost is higher because the variables follow the same rule for different uncertain scenarios. To adapt to the changes of uncertainty sets in different periods, the piecewise linear decision rules are proposed in [23]. Nevertheless, it is still challenging to provide customized ADRs for different realizations of uncertain variables in the same period. Hence, it is imperative to develop optimization techniques to obtain reliable and economic scheduling strategies for energy system operations with variable REG.

To sum up, the following issues remain to be addressed.

1) The duration of AEL state transition is assumed constant in the existing literature, which restricts the operational flexibility of IEHHSs.

2) The RO method guarantees a reliable but conservative operation of IEHHS with variable REG, which increases the IEHHS operating cost.

To overcome these deficiencies, this paper proposes a robust scheduling of IEHHS.

The main contributions of this paper are summarized as follows.

1) A flexible operation model of IEHHSs coordinating the AELs, active distribution networks (ADNs), and DHNs is established. The bidirectional heat exchange (BHE) between AELs and DHNs is proposed, which not only enables the waste heat recovery for district heating but also accelerates the thermal dynamics in AELs. Accordingly, the duration of AEL state transition is reduced, and the operational flexibility of IEHHSs is enhanced.

2) A novel ADR, i.e., multi-affine decision rule (MADR), is proposed to solve the two-stage RO problem for the scheduling of IEHHSs. The uncertainty set of REG is proposed as a union of multiple subsets, and MADR is developed to provide different ADRs for each uncertainty subset. Compared with the traditional ADR, the MADR reduces the IEHHS operating costs while guaranteeing the reliability of scheduling strategies for IEHHS.

The comparisons of literature related to the scheduling of IEHHSs are summarized in Table I.

TABLE I
COMPARISON OF LITERATURE RELATED TO SCHEDULING OF IEHHSs

Reference	Coupling of DHNs and AELs	AEL state transitions	Scheduling method	MADR
[11]	Unidirectional	×	RO	×
[14]	Unidirectional	×	MPC	×
[24]	Unidirectional	√	MILP	×
This paper	Bidirectional	√	Two-stage RO	√

Note: MPC is short for model predictive control; and MILP is short for mixed-integer linear programming.

The rest of this paper is organized as follows. The IEHHS is modeled in Section II. The two-stage RO problem for IEHHS operation is formulated in Section III. The solution method is proposed in Section IV. Case studies are given in Section V, followed by conclusions in Section VI.

II. IEHHS MODELING

A. IEHHS Configuration

Figure 1 illustrates the energy flow in IEHHS, where ADNs and DHNs are coupled via AELs.

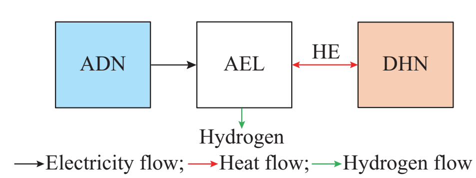

Fig. 1. Diagram of energy flow in IEHHS.

The electricity from ADNs integrated with REG is utilized to produce hydrogen. Hence, the uncertainty of REG needs to be managed for efficient IEHHS operation. Moreover, the heat exchange between AELs and DHNs is transferred bidirectionally through a heat exchanger (HE) considering that:

1) The optimal production temperature of AELs is about 90 °C, which is usually higher than the temperature of return water of DHNs.

2) The temperature of supply water of DHNs lies in the range of 80-110 °C, which can heat up electrolytes. The temperature difference in AELs and DHNs enables the spontaneous heat exchange through HEs. As a result, the exhaust heat from water electrolysis can be recovered for district heating, and the heat from DHNs can also accelerate the AEL thermal process. The detailed models of AEL, ADN, and DHN are given in the following.

B. Model of AEL

1) AEL States

The AEL states are commonly divided into off, standby, and production states, which are denoted as s_1, s_2, and s_3, respectively, as shown in Fig. 2(a) [8], [24]. In the off state, the AEL temperature is below the minimum working temperature, and the AEL power is zero. In the standby state, the temperature is maintained within the operational range, and the AEL power is smaller than the minimum operating power. In the production state, AELs are operated within the allowable temperature and power ranges. The transitions between different states include cold start, hot start, standby, and shut-down. The cold start usually takes tens of minutes due to the high thermal inertia of industrial AELs [25], while other transitions can be accomplished within a few minutes. Therefore, the time of cold start processes needs to be considered in the hourly IEHHS scheduling, while the time consumption of other transitions is ignored.

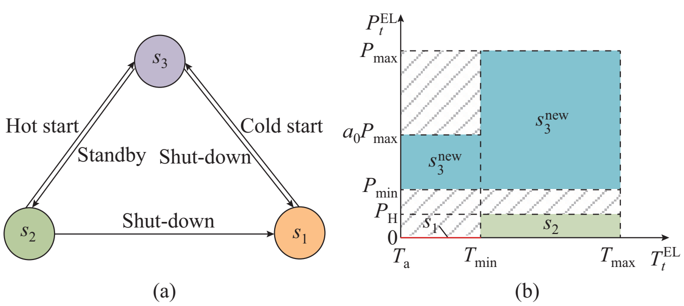

Fig. 2. Illustration of AEL states. (a) Transitions between AEL states. (b) New model of AEL states.

In the existing literature, the time of cold start is set to be a constant, which neglects that it can be reduced by accelerating the AEL thermal process. Here, we design a new model of AEL states based on the AEL temperature and power, which enables more flexible operations by utilizing the heat exchange between AELs and DHNs.

Figure 2(b) depicts the new model of AEL states. Considering that AELs keep working in the cold start process, a new state s_3^{new} is established to contain both cold start and production states. As shown in Fig. 2(b), the left part of s_3^{new} represents the cold start process, where the power is limited by a start-up coefficient a_0 $(0<a_0<1)$ [25]. When the temperature rises within the operational range $[T_{min}, T_{max}]$, AELs are switched into the production state, indicated by the right part of s_3^{new}. Hence, the AEL states are modeled as:

$$s_{1,t}=\begin{cases}1 & T_a\le T_t^{EL}<T_{min}, P_t^{EL}=0\\ 0 & \text{others}\end{cases} \tag{1a}$$

$$s_{2,t}=\begin{cases}1 & T_{min}\le T_t^{EL}<T_{max}, 0\le P_t^{EL}\le P_H\\ 0 & \text{others}\end{cases} \tag{1b}$$

$$s_{3,t}^{new}=\begin{cases}1 & T_a<T_t^{EL}\le T_{max}, P_{min}<P_t^{EL}\le a_t P_{max}\\ 0 & \text{others}\end{cases} \tag{1c}$$

$$a_t=\begin{cases}a_0 & T_t^{EL}<T_{min}\\ 1 & T_{min}\le T_t^{EL}\le T_{max}\end{cases} \tag{1d}$$

$$s_{1,t}+s_{2,t}+s_{3,t}^{new}=1 \tag{1e}$$

where subscript t is the index of time; T_a is the ambient temperature; P_t^{EL} and T_t^{EL} are the AEL power and temperature, respectively; P_H is the maximum power in the standby state; a_t is the scaling factor in the production state; P_{min} and P_{max} are the minimum and maximum operating power, respectively; and T_{min} and T_{max} are the minimum and maximum AEL temperatures, respectively.

2) BHE Between AEL and DHN

To improve the operational flexibility of AELs restricted by high thermal inertia, the BHE between AELs and DHNs is proposed, as shown in Fig. 3. The heat transfer direction is controlled by two valves, denoted as V1 and V2. When V1 is open and V2 is closed, the heat from AELs is transferred to the return water of DHNs; when V1 is closed and V2 is open, the supply water with high temperature flows into BHEs for heating the electrolyte.

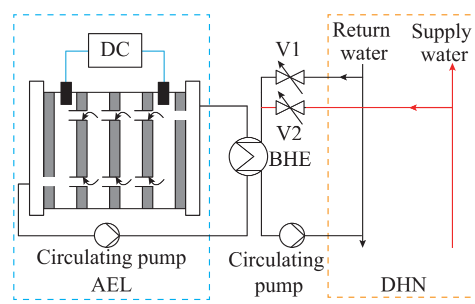

Fig. 3. Illustration of BHE between AEL and DHN.

In this way, the heat is exchanged flexibly between AELs and DHNs, which is formulated as:

$$k_t^{V1}=\begin{cases}1 & H_t^{HE}\ge 0\\ 0 & H_t^{HE}<0\end{cases} \tag{2a}$$

$$k_t^{V2}=1-k_t^{V1} \tag{2b}$$

where H_t^{HE} is the exchanged heat with the positive direction from AELs to DHNs; and k_t^{V1} and k_t^{V2} are the binary variables denoting the switching states of valves V1 and V2, respectively.

3) AEL System Modeling

The relationship between the power consumption of AEL and hydrogen production is modeled as:

$$P_t^{EL} = N_c P_t^{cell} \tag{3a}$$

$$I_t^{EL} = A_m (P_t^{cell} - k_a T_t^{EL} - k_c) k_b^{-1} \tag{3b}$$

$$n_t^{H2} = N_c I_t^{EL} \Delta t (zF)^{-1} \tag{3c}$$

$$s_{3,t}^{new} P_{min}^{EL} \leq P_t^{EL} \leq a_t^{EL} s_{3,t}^{new} P_{max}^{EL} \tag{3d}$$

where P_t^{cell} is the power consumed in each cell; N_c is the number of cells; k_a, k_b, and k_c are the coefficients for the approximated linear model of AEL; I_t^{EL} is the current of AEL; A_m is the membrane area; n_t^{H2} is the hydrogen production; Δt is the time interval; F is the Faraday constant; z is the number of transferred electrons; and P_{min}^{EL} and P_{max}^{EL} are the minimum and maximum power of AEL, respectively.

Constraints (3a) - (3c) represent the approximated linear AEL model [24]. Constraint (3d) provides the limits of AEL power.

The power consumption of AEL P_t^{AC} is calculated as:

$$P_t^{AC} = P_t^{EL} + P_t^{BoP} \tag{4a}$$

$$P_t^{BoP} = s_{2,t} H_t^{dis} + \gamma_{BoP} s_{3,t}^{new} P_t^{EL} \tag{4b}$$

where P_t^{BoP} is the power consumed by balance of plant (BoP), which contains circulating pumps, temperature regulation, gas purification systems, etc. [26]-[28]; H_t^{dis} is the heat dissipation of AEL; and γ_{BoP} is a proportional factor.

Constraint (4a) gives the total power consumption. Constraint (4b) indicates that the power consumed by BoP is proportional to AEL power when AEL is working in the production state. P_t^{BoP} is used mainly to maintain the AEL temperature within operational ranges when AEL is in the standby state.

The heat and temperature constraints of AEL are given by:

$$H_t^{EL} = P_t^{EL} - N_c u_{tn} I_t^{EL} \tag{5a}$$

$$H_t^{dis} = (T_t^{EL} - T_a) R_{EL}^{-1} \tag{5b}$$

$$T_{t+1}^{EL} = T_t^{EL} + \Delta t C_{EL}^{-1} [H_t^{EL} - H_t^{dis} - (k_t^{V2} - k_t^{V1}) H_t^{HE}] \tag{5c}$$

$$T_{min} \leq T_t^{EL} \leq T_{max} \tag{5d}$$

$$0 \leq (k_t^{V2} - k_t^{V1}) H_t^{HE} \leq H_{max}^{EL} (T_{max} - T_a)^{-1} [k_t^{V1} (T_t^s - T_t^{EL}) + k_t^{V2} (T_t^{EL} - T_t^r)] \tag{5e}$$

where H_t^{HE} is the heat generated along with hydrogen production; u_{tn} is the thermal neutral voltage; C_{EL} and R_{EL} are the heat capacity and resistance of AEL, respectively; H_{max}^{EL} is the maximum heat dissipation of AEL; and T_t^s and T_t^r are the temperatures of supply and return water for DHN nodes connected with HEs, respectively.

Constraint (5a) shows that the heat is the difference between the utilized electricity and the internal energy for producing hydrogen. Constraint (5b) indicates that the heat dissipation is proportional to the temperature difference between AELs and their surroundings. Constraint (5c) gives the heat balance equation. Constraint (5d) gives the temperature limits. Constraint (5e) shows that the temperature difference between hot and cold sides limits the heat through HEs.

C. Model of ADN

The operation constraints of combined heat and power (CHP) plants are given as:

$$[\boldsymbol{a}_{CHP} \quad \boldsymbol{b}_{CHP}][P_t^{CHP} \quad H_t^{CHP}]^T \leq k_t^{CHP} \boldsymbol{d}_{CHP} \tag{6a}$$

$$n_t^{NG} = P_t^{CHP} \eta_{CHP}^{-1} L_{NG}^{-1} \tag{6b}$$

$$Q_t^{CHP} = \lambda_{CHP} P_t^{CHP} \tag{6c}$$

where P_t^{CHP} and H_t^{CHP} are the active power and heat of CHP plant, respectively; $\boldsymbol{a}_{CHP}$, $\boldsymbol{b}_{CHP}$, and $\boldsymbol{d}_{CHP}$ are the vectors characterizing the feasible region regarding the electric power and heat of CHP plant [11]; k_t^{CHP} is a binary variable to indicate the status of CHP plant; n_t^{NG} is the consumption rate of natural gas; η_{CHP} is the efficiency of CHP plant; L_{NG} is the low heat value of natural gas; Q_t^{CHP} is the reactive power of CHP plant; and λ_{CHP} is the proportion coefficient of Q_t^{CHP} with respect to P_t^{CHP}.

The power flows and nodal voltages in ADN are modeled based on the linear DistFlow model [29] as:

$$\sum_{k \in \delta(j)} P_{jk,t} = P_{j,t}^{RE} + P_{j,t}^{CHP} - P_{j,t}^{AC} - P_{j,t}^{D} \tag{7a}$$

$$\sum_{k \in \delta(j)} Q_{jk,t} = Q_{j,t}^{RE} + Q_{j,t}^{CHP} - Q_{j,t}^{D} \tag{7b}$$

$$V_{j,t} = V_{i,t} - 2(r_{ij} P_{ij,t} + x_{ij} Q_{ij,t}) \tag{7c}$$

$$0 \leq P_{j,t}^{RE} \leq P_{j,t}^{0} \tag{7d}$$

$$Q_{j,min}^{RE} \leq Q_{j,t}^{RE} \leq Q_{j,max}^{RE} \tag{7e}$$

$$V_{min} \leq V_{j,t} \leq V_{max} \tag{7f}$$

where i, j, and k are the indices of nodes; $P_{jk,t}$ and $Q_{jk,t}$ are the active and reactive power flows through line jk at time t, respectively; $\delta(j)$ is the set of ending points of branches connecting to node j; $P_{j,t}^{RE}$ and $Q_{j,t}^{RE}$ are the active and reactive power of REG, respectively; $P_{j,t}^{D}$ and $Q_{j,t}^{D}$ are the active and reactive power of loads, respectively; r_{ij} and x_{ij} are the resistance and reactance of line ij, respectively; $V_{j,t}$ is the squared voltage magnitude of node j; $P_{j,t}^{0}$ is the maximum active power of REG connecting to node j; $Q_{j,min}^{RE}$ and $Q_{j,max}^{RE}$ are the minimum and maximum reactive power of REG at node j, respectively; and V_{min} and V_{max} are the minimum and maximum squared voltage magnitudes, respectively.

D. Model of DHN

The HE constraints are given as:

$$C_t^{HE} = \min\{m_c C_c, m_h C_h\} \tag{8a}$$

$$H_{max} = C_t^{HE} (T_t^{h,in} - T_t^{c,in}) \tag{8b}$$

$$H_t^{HE} = \eta_{HE} H_{max} \tag{8c}$$

where C_h and C_c are the heat capacities on the hot and cold sides of HEs, respectively; m_h and m_c are the mass flows on the hot and cold sides of HEs, respectively; C_t^{HE} is the actual heat capacity; $T_t^{h,in}$ and $T_t^{c,in}$ are the input temperatures of mass flows on the hot and cold sides, respectively; H_{max} is the maximum exchanged heat power; and η_{HE} is an efficiency parameter that determines the actual heat transmitted between hot and cold sides.

The model of DHN with constant mass flows is presented in (9) [30], and the limits of node temperature and branch mass flows are given in (10).

$$\boldsymbol{m}_{t,b}=\boldsymbol{A}_{\mathrm{DHN}}^{\mathrm{T}}\boldsymbol{m}_{t,n} \tag{9a}$$

$$T_{t,b,\mathrm{end}}=\gamma_{\mathrm{loss}}L_b(T_{t,b,\mathrm{start}}-T_{\mathrm{a}})+T_{\mathrm{a}} \tag{9b}$$

$$\left(\sum_{j\in\delta(i)}m_{t,j}\right)T_{t,i}=\sum_{j\in\delta(i)}m_{t,j}T_{t,j} \tag{9c}$$

$$H_{t,i}=C_{\mathrm{w}}m_{t,i}(T_{t,i}^{\mathrm{s}}-T_{t,i}^{\mathrm{r}}) \tag{9d}$$

$$T_{\min}^{\mathrm{s}}\le T_{t,i}^{\mathrm{s}}\le T_{\max}^{\mathrm{s}} \tag{10a}$$

$$T_{\min}^{\mathrm{r}}\le T_{t,i}^{\mathrm{r}}\le T_{\max}^{\mathrm{r}} \tag{10b}$$

$$\boldsymbol{m}_{\min}\le\boldsymbol{m}_{t,b}\le\boldsymbol{m}_{\max} \tag{10c}$$

where $\boldsymbol{m}_{t,b}$ and $\boldsymbol{m}_{t,n}$ are the mass flow vectors of branch and node, respectively; $\boldsymbol{A}_{\mathrm{DHN}}$ is the incidence matrix; $T_{t,b,\mathrm{start}}$ and $T_{t,b,\mathrm{end}}$ are the temperatures of starting and ending points of branch, respectively; γ_{loss} is the temperature drop coefficient per unit distance; L_b is the length of branch; $m_{t,j}$ is the mass flow of node j; $T_{t,i}$ is the temperature of node i; $T_{t,i}^{\mathrm{s}}$ and $T_{t,i}^{\mathrm{r}}$ are the temperatures of node i regarding supply and return networks, respectively; $H_{t,i}$ is the heat demand of node i; $\boldsymbol{m}_{\max}$ and $\boldsymbol{m}_{\min}$ are the upper and lower limits of mass flow for branch, respectively; $T_{\max}^{\mathrm{s}}$ and $T_{\min}^{\mathrm{s}}$ are the upper and lower temperature limits of supply network, respectively; and $T_{\max}^{\mathrm{r}}$ and $T_{\min}^{\mathrm{r}}$ are the upper and lower temperature limits of return network, respectively.

Constraint (9a) gives the relationship between the mass flows of branch and node. Constraint (9b) gives the model of the water temperature at the starting and ending points of branches with linear loss approximation [11]. Constraint (9c) gives the nodal temperature after the branch confluence. Constraint (9d) gives the nodal heat demand and temperature model. Constraint (10) gives the upper and lower limits of temperature and mass flows.

III. Two-stage RO Problem for IEHHS Operation

This section presents a two-stage RO problem for coordinating day-ahead and intra-day operations with uncertain REG.

A. Day-ahead Operation Problem

The day-ahead operation aims to minimize the IEHHS operating cost for a typical profile of REG, where the objective function is given as:

$$\min\sum_{t=1}^{t_{\max}}(\lambda_{\mathrm{NG}}n_t^{\mathrm{NG}}+\lambda_0^+P_t^{0+}-\lambda_0^-P_t^{0-}-\lambda_{\mathrm{H2}}n_t^{\mathrm{H2}}) \tag{11}$$

where $t_{\max}$ is the scheduling period; P_t^{0+} and P_t^{0-} are the power imported from and exported to upstream grids, respectively; and λ_{NG}, λ_0^+, λ_0^-, and λ_{H2} are the price coefficients of natural gas, imported power, exported power, and hydrogen, respectively.

The objective function includes the operating cost of CHP plants, the cost of importing power from upstream grids, the revenue of exporting power to upstream grids, and the revenue of selling hydrogen. The produced hydrogen is assumed to be sold out, and thus the revenue of selling hydrogen is proportional to the produced hydrogen.

The day-ahead decisions include: ① states, electric power, current, dissipated heat, and temperature of AELs; ② states and transferred heat of HEs; ③ states, electric power, and heat in CHP plants; ④ power imported from or exported to upstream grids; ⑤ active and reactive power of REGs; and ⑥ line flows and nodal voltages of ADNs. Denote the vector of day-ahead decision variables at time t as $\boldsymbol{x}_t$:

$$\boldsymbol{x}_t=[s_t^1,s_t^2,s_t^{3,\mathrm{new}},k_t^{\mathrm{V1}},k_t^{\mathrm{V2}},k_t^{\mathrm{CHP}},P_t^{0+},P_t^{0-},P_t^{\mathrm{EL}},P_t^{\mathrm{RE}},P_t^{\mathrm{CHP}},\\ H_t^{\mathrm{CHP}},H_t^{\mathrm{HE}},H_t^{\mathrm{dis}},I_t^{\mathrm{EL}},T_t^{\mathrm{EL}},P_{t,jk},Q_{t,jk},Q_{j,t}^{\mathrm{CHP}},Q_{r,j,t},V_{j,t}] \tag{12}$$

The day-ahead operation constraints include those of AEL ((1)-(5)), CHP plant ((6)), ADN ((7)), HE ((8)), and DHN ((9) and (10)). By the big-M method and the if-then-else rules, (1a)-(1c), (2a), (3d), and (5e) are converted into linear constraints. Hence, the day-ahead operation problem is expressed in a compact form as:

$$\min\boldsymbol{a}^{\mathrm{T}}\boldsymbol{x} \tag{13a}$$

s.t.

$$\boldsymbol{Ax}\le\boldsymbol{c} \tag{13b}$$

where $\boldsymbol{A}$, $\boldsymbol{a}$, and $\boldsymbol{c}$ are the coefficients derived from (1)-(10).

B. Intra-day Operation Problem

At the intra-day operation stage, the electric power and heat of AELs and CHP plants, the heat through HEs, and the electric power imported from and exported to upstream grids are adjusted to consider the variations of REG. Besides, the off, standby, and production states of AELs, start and stop states of CHP plants, and heat exchange direction through HEs remain the same as those at the day-ahead operation stage due to the relatively long transition time between different states. Hence, given the day-ahead scheduling, the intra-day operation aims to minimize the re-dispatch cost in the worst scenarios, where the objective function is given as:

$$\max_{\boldsymbol{\xi}\in U}\min_{\boldsymbol{y}}\sum_{t=1}^{t_{\max}}(\Delta C_t^0+\Delta C_t^{\mathrm{CHP}}+\Delta C_t^{\mathrm{CUR}}-\Delta C_t^{\mathrm{H2}}) \tag{14a}$$

$$\Delta C_t^0=\lambda_0^+\Delta P_t^{0,\mathrm{up}}-\lambda_0^-\Delta P_t^{0,\mathrm{dn}} \tag{14b}$$

$$\Delta C_t^{\mathrm{CHP}}=\lambda_{\mathrm{NG}}\Delta P_t^{\mathrm{CHP}}\Delta t(\eta_{\mathrm{CHP}}L_{\mathrm{NG}})^{-1} \tag{14c}$$

$$\Delta C_t^{\mathrm{CUR}}=\lambda_{\mathrm{CUR}}\sum_{r=1}^{R}(P_{r,t}^0+\xi_{r,t}-P_{r,t}^{\mathrm{RE}}-\Delta P_{r,t}^{\mathrm{RE}}) \tag{14d}$$

$$\Delta C_t^{\mathrm{H2}}=\lambda_{\mathrm{H2}}N_{\mathrm{c}}\Delta I_t^{\mathrm{EL}}(zF)^{-1} \tag{14e}$$

where ΔC_t^0 is the cost of power adjustments from upstream grid; $\Delta C_t^{\mathrm{CHP}}$ is the re-dispatch cost of CHP plants; $\Delta C_t^{\mathrm{CUR}}$ is the cost of curtailing REG; ΔC_t^{H2} is the intra-day revenue for selling hydrogen; λ_{CUR} is the price of curtailing REG; $\Delta P_t^{0,\mathrm{up}}$ and $\Delta P_t^{0,\mathrm{dn}}$ are the upward and downward adjustments of power from upstream grid, respectively; $\Delta P_t^{\mathrm{CHP}}$ is the adjustment of electric power of CHP plants; $P_{r,t}^0$ is the day-ahead predicted output of REG r; $\Delta P_{r,t}^{\mathrm{RE}}$ and $\xi_{r,t}$ are the power utilization and variation of REG r at the intra-day operation stage, respectively; R is the number of REGs; ΔI_t^{EL} is the current adjustment of AEL; $\boldsymbol{y}$ is the vector of intra-day decision variables; and U is the uncertainty set to characterize the variations of REG $\boldsymbol{\xi}$.

The intra-day operation constraints are given as:

$$\Delta T_t^{\mathrm{EL}}=T_0^{\mathrm{EL}}-T_t^{\mathrm{EL}}+\frac{\Delta t}{C_{\mathrm{EL}}}\sum_{\tau=1}^{t-1}[P_\tau^{\mathrm{EL}}+\Delta P_\tau^{\mathrm{EL}}-N_{\mathrm{c}}u_{\mathrm{th}}(I_\tau^{\mathrm{EL}}+\Delta I_\tau^{\mathrm{EL}})-H_\tau^{\mathrm{dis}}-\Delta H_\tau^{\mathrm{dis}}-H_\tau^{\mathrm{HE}}-\Delta H_\tau^{\mathrm{HE}}] \tag{15a}$$

$$\Delta I_t^{\mathrm{EL}}=A_{\mathrm{m}}k_{\mathrm{b}}^{-1}(P_t^{\mathrm{EL}}+\Delta P_t^{\mathrm{EL}})-k_{\mathrm{a}}(T_t^{\mathrm{EL}}+\Delta T_t^{\mathrm{EL}})-k_{\mathrm{c}}-I_t^{\mathrm{EL}} \tag{15b}$$

$$s_{3,t}^{\mathrm{new}}P_{\min}^{\mathrm{EL}}\le P_t^{\mathrm{EL}}+\Delta P_t^{\mathrm{EL}}\le a_t^{\mathrm{EL}}s_{3,t}^{\mathrm{new}}P_{\max}^{\mathrm{EL}} \tag{15c}$$

$$(s_{2,t}+s_{3,t}^{\mathrm{new}})T_{\min}\le T_t^{\mathrm{EL}}+\Delta T_t^{\mathrm{EL}}\le T_{\max} \tag{15d}$$

$$0\le(k_t^{\mathrm{V2}}-k_t^{\mathrm{V1}})H_{t,\mathrm{R}}^{\mathrm{HE}}\le H_{\max}^{\mathrm{EL}}(T_{\max}-T_{\mathrm{a}})^{-1}[k_t^{\mathrm{V1}}(T_t^{\mathrm{s}}-T_{t,\mathrm{R}}^{\mathrm{EL}})+k_t^{\mathrm{V2}}(T_t^{\mathrm{EL}}+\Delta T_t^{\mathrm{EL}}-T_t^{\mathrm{r}})] \tag{16}$$

$$\begin{bmatrix}\boldsymbol{a}_{\mathrm{CHP}} & \boldsymbol{b}_{\mathrm{CHP}}\end{bmatrix}\begin{bmatrix}P_t^{\mathrm{CHP}}+\Delta P_t^{\mathrm{CHP}}\\ H_t^{\mathrm{CHP}}+\Delta H_t^{\mathrm{CHP}}\end{bmatrix}\le k_t^{\mathrm{CHP}}\boldsymbol{d}_{\mathrm{CHP}} \tag{17}$$

$$0\le P_{j,t}^{\mathrm{RE}}+\Delta P_{j,t}^{\mathrm{RE}}\le P_{j,t}^0+\xi_{j,t} \tag{18a}$$

$$\sum_{k\in\delta(j)}P_{jk,t,\mathrm{R}}=-(P_{j,t}^{\mathrm{AC}}+\Delta P_{j,t}^{\mathrm{AC}})-P_{j,t}^{\mathrm{D}}+(P_{j,t}^{\mathrm{RE}}+\Delta P_{j,t}^{\mathrm{RE}}+P_{j,t}^{\mathrm{CHP}}+\Delta P_{j,t}^{\mathrm{CHP}}) \tag{18b}$$

$$\sum_{k\in\delta(j)}Q_{jk,t,\mathrm{R}}=Q_{j,t}^{\mathrm{CHP}}+\Delta Q_{j,t}^{\mathrm{CHP}}+Q_{j,t}^{\mathrm{RE}}+\Delta Q_{j,t}^{\mathrm{RE}}-Q_{j,t}^{\mathrm{D}} \tag{18c}$$

$$V_{j,t,\mathrm{R}}=V_{i,t,\mathrm{R}}-2(r_{ij}P_{ij,t,\mathrm{R}}+x_{ij}Q_{ij,t,\mathrm{R}}) \tag{18d}$$

$$0\le P_t^{0+}+\Delta P_t^{0,\mathrm{up}}\le P_{\max}^{0+} \tag{18e}$$

$$0\le P_t^{0-}+\Delta P_t^{0,\mathrm{dn}}\le P_{\max}^{0-} \tag{18f}$$

$$P_{\min}^0\le P_t^{0+}-P_t^{0-}+\Delta P_t^{0,\mathrm{up}}-\Delta P_t^{0,\mathrm{dn}}\le P_{\max}^0 \tag{18g}$$

$$Q_{j,\min}^{\mathrm{RE}}\le Q_{j,t}^{\mathrm{RE}}+\Delta Q_{j,t}^{\mathrm{RE}}\le Q_{j,\max}^{\mathrm{RE}} \tag{18h}$$

$$V_{\min}\le V_{t,i,\mathrm{R}}\le V_{\max} \tag{18i}$$

where the symbol Δ represents the adjustment value of the corresponding variable; the subscript R denotes the variables at the intra-day stage without adjustments; T_0^{EL} is the initial AEL temperature; τ is the counting flag; $H_{t,R}^{\mathrm{HE}}$ is the intra-day heat exchange; $P_{\max}^{0+}$ and $P_{\max}^{0-}$ are the maximum power imported from and exported to upstream grids, respectively; and $P_{\min}^0$ and $P_{\max}^0$ are the minimum and maximum net power from upstream grids, respectively.

Constraint (15) gives the AEL limits at the intra-day operation stage. Constraint (16) gives the limits of exchanged heat through HEs at the intra-day operation stage. Constraint (17) gives the intra-day operation limit of CHP plants. Constraint (18) gives the intra-day operation limit of ADNs.

Let $\boldsymbol{y}_t$ represent the vector of intra-day decision variables at time t:

$$\boldsymbol{y}_t=[\Delta P_t^{0+},\Delta P_t^{0-},\Delta P_t^{\mathrm{EL}},\Delta P_t^{\mathrm{RE}},\Delta P_t^{\mathrm{CHP}},\Delta H_t^{\mathrm{CHP}},H_{t,\mathrm{R}}^{\mathrm{HE}},\Delta H_t^{\mathrm{dis}},\Delta I_t^{\mathrm{EL}},\Delta T_t^{\mathrm{EL}},P_{jk,t,\mathrm{R}},Q_{jk,t,\mathrm{R}},\Delta Q_{j,t}^{\mathrm{CHP}},\Delta Q_t^{\mathrm{RE}},V_{i,t,\mathrm{R}}] \tag{19}$$

Because (14)-(18) are linear, the intra-day operation problem can be formulated in a compact form as:

$$\max_{\boldsymbol{\xi}\in U}\min_{\boldsymbol{y}}\boldsymbol{b}^{\mathrm{T}}\boldsymbol{y} \tag{20a}$$

s.t.

$$\boldsymbol{Bx}+\boldsymbol{Cy}+\boldsymbol{D\xi}\le\boldsymbol{d} \tag{20b}$$

where $\boldsymbol{B}$, $\boldsymbol{C}$, $\boldsymbol{D}$, $\boldsymbol{b}$, and $\boldsymbol{d}$ are the coefficient matrices or vectors derived from (15)-(18).

C. Compact Form of Day-ahead and Intra-day Operation Problem

Finally, the coordinated day-ahead and intra-day operation problem is established as a two-stage RO problem. The day-ahead operation determines the states, electric power, and heat of AELs, CHP plants, and HEs, as well as the power imported from or exported to upstream grids. The intra-day operation adjusts the power of AELs, CHP plants, and HEs, as well as that from upstream grids to follow REG variations. The compact form of the two-stage RO problem is presented as:

$$\begin{cases}F_{\mathrm{c}}=\min\limits_{\boldsymbol{x}}\left\{\boldsymbol{a}^{\mathrm{T}}\boldsymbol{x}+\max\limits_{\boldsymbol{\xi}\in U}\min\limits_{\boldsymbol{y}}\boldsymbol{b}^{\mathrm{T}}\boldsymbol{y}\right\}\\ \text{s.t. (13a), (20b)}\end{cases} \tag{21}$$

IV. Solution Method

A. MADR

The ADR is an effective method to solve the two-stage RO problem and provides scheduling strategies for intra-day operations [18], [31]. Specifically, the second-stage decision variables of this RO problem are proposed as affine functions of random variables $\boldsymbol{\xi}$, as stated below:

$$\boldsymbol{y}=\boldsymbol{y}_0+\boldsymbol{Y\xi} \tag{22}$$

where $\boldsymbol{y}_0$ is the constant matrix; and $\boldsymbol{Y}$ is the coefficient matrix of the first-order term. Then, the two-stage RO problem (21) becomes:

$$F_{\mathrm{c}}^{\mathrm{SA}}=\min_{\boldsymbol{x},\boldsymbol{y}_0,\boldsymbol{Y}}\left\{\boldsymbol{a}^{\mathrm{T}}\boldsymbol{x}+\max_{\boldsymbol{\xi}\in U}\boldsymbol{b}^{\mathrm{T}}(\boldsymbol{y}_0+\boldsymbol{Y\xi})\right\} \tag{23}$$

Here, (22) is denoted as the single-affine decision rule (SADR), which may lead to conservative scheduling strategies, because the second-stage decisions follow the same rule for any scenario in uncertainty sets.

To reduce the conservatism of SADR, we propose the MADR to provide different decision rules for different realizations. Assume that the uncertainty set U consists of N subsets $U_1, U_2, \ldots, U_N$. For subset U_i, the second-stage decision variables are expressed as:

$$\boldsymbol{y}=\boldsymbol{y}_{i,0}+\boldsymbol{Y}_i\,\boldsymbol{\xi} \tag{24}$$

where $\boldsymbol{y}_{i,0}$ and $\boldsymbol{Y}_i$ are the affine coefficients for subset U_i.

Next, problem (23) is transformed into:

$$F_{\mathrm{c}}^{\mathrm{MA}}=\min_{\boldsymbol{x},\boldsymbol{y}_{i,0},\boldsymbol{Y}_i}\left\{\boldsymbol{a}^{\mathrm{T}}\boldsymbol{x}+\max_{i\in\{1,2,\ldots,N\}}\max_{\boldsymbol{\xi}\in U_i}\boldsymbol{b}^{\mathrm{T}}(\boldsymbol{y}_{i,0}+\boldsymbol{Y}_i\,\boldsymbol{\xi})\right\} \tag{25}$$

The superiority of MADR over SADR in solving the two-stage RO problem is shown by Theorem 1 in Supplementary Material A.

B. Uncertainty Set Model

First, we divide the REG samples into multiple clusters using the multivariate time-series K-means clustering method, which establishes clusters iteratively. In the n^{th} iteration, the clusters are given as:

$$S_{n,i}=\arg\min_{S}\sum_{\boldsymbol{\xi}\in\Xi}\sum_{z=1}^{Z}\|\boldsymbol{c}_{n,i}-\boldsymbol{\xi}_z\|^2\quad i\in\{1,2,\ldots,N\} \tag{26}$$

where $\boldsymbol{c}_{n,i}$ is the centroid of cluster i in the n^{th} iteration; $S_{n,i}$ is the set of samples belonging to cluster i in the n^{th} iteration; $\boldsymbol{\xi}_z$ is the vector of time-series samples for REG power in the z^{th} day; $\varXi$ is the set of samples; and Z is the number of days.

The cluster centroid is calculated by:

$$\boldsymbol{c}_{n+1,i}=\frac{1}{n_i}\sum_{\xi\in S_i}\boldsymbol{\xi}\quad i\in\{1,2,...,N\} \tag{27}$$

where n_i is the number of samples in cluster i. The clusters are updated by solving (26) and (27) iteratively until they are not changed.

Then, for each cluster, the uncertainty subset is modeled as a polyhedron:

$$U_i=\{\boldsymbol{\xi}|\boldsymbol{W}_i\boldsymbol{\xi}\leq\boldsymbol{w}_i\}\quad i\in\{1,2,...,N\} \tag{28}$$

where $\boldsymbol{W}_i$ is a coefficient matrix; and $\boldsymbol{w}_i$ is a vector derived from polyhedral uncertainty subset.

Finally, the uncertainty set is established as a union of different uncertainty subsets:

$$U=\bigcup_{i=1}^{N}U_i \tag{29}$$

C. MADR-based Solution Method

Based on the uncertainty set U, the two-stage RO problem (21) is formulated as:

$$\begin{cases}\min\limits_{\boldsymbol{x}}\left\{\boldsymbol{a}^{\mathrm{T}}\boldsymbol{x}+\max\limits_{i\in\{1,2,...,N\}}\max\limits_{\xi\in U_i}\min\limits_{\boldsymbol{y}}\sum\boldsymbol{b}^{\mathrm{T}}\boldsymbol{y}\right\}\\ \text{s.t. (13b), (20b), (28)}\end{cases} \tag{30}$$

Utilizing the MADR for solving (30), the second-stage decision variables $\boldsymbol{y}$ are divided into two categories. The variables in the first category, including $\{\Delta P_t^{0+}$, ΔP_t^{EL}, $\Delta P_{r,t}$, $\Delta P_t^{\mathrm{CHP}}$, $\Delta H_t^{\mathrm{CHP}}$, $\Delta H_{t,}^{\mathrm{dis}}$, $H_{t,R}^{\mathrm{HE}}\}$, are replaced with the affine functions of random variables. The second category includes the rest of the second-stage decision variables, which are expressed as functions of those in the first category and random variables. The second-stage decision variables are given in Supplementary Material B, and all of them can be presented in the form of affine functions:

$$\boldsymbol{y}=\boldsymbol{M}_i\boldsymbol{\xi}+\boldsymbol{m}_i \tag{31}$$

where $\boldsymbol{M}_i$ and $\boldsymbol{m}_i$ are the matrix and vector of affine coefficients for subset U_i, respectively. By replacing $\boldsymbol{y}$ with (31), the problem (30) becomes:

$$\min_{\boldsymbol{x},\boldsymbol{M}_i,\boldsymbol{m}_i}\left\{\boldsymbol{a}^{\mathrm{T}}\boldsymbol{x}+\max_{i\in\{1,2,...,N\}}\max_{\xi\in U_i}\{\boldsymbol{b}^{\mathrm{T}}\boldsymbol{M}_i\boldsymbol{\xi}+\boldsymbol{b}^{\mathrm{T}}\boldsymbol{m}_i\}\right\} \tag{32a}$$

s.t.

$$\boldsymbol{Ax}\leq\boldsymbol{c} \tag{32b}$$

$$(\boldsymbol{CM}_i+\boldsymbol{D})\boldsymbol{\xi}\leq\boldsymbol{d}-\boldsymbol{Bx}-\boldsymbol{Cm}_i\quad\forall\boldsymbol{\xi}\in U_i, i\in\{1,2,\ldots,N\} \tag{32c}$$

Then, the robust constraint (32c) is reformulated into (33) by the duality theory. The duality transformation is given in Supplementary Material C.

$$\boldsymbol{w}_i^{\mathrm{T}}\boldsymbol{\mu}_{1,i}\leq\boldsymbol{d}-\boldsymbol{Bx}-\boldsymbol{Cm}_i \tag{33a}$$

$$\boldsymbol{W}_i^{\mathrm{T}}\boldsymbol{\mu}_{1,i}=(\boldsymbol{CM}_i+\boldsymbol{D})^{\mathrm{T}} \tag{33b}$$

$$\boldsymbol{\mu}_{1,i}\geq\boldsymbol{0} \tag{33c}$$

where $\boldsymbol{\mu}_{1,i}$ is the vector for dual variables of (32c).

The inner maximum problem of (32a) is converted into a minimum problem using the duality theory:

$$\min_{\boldsymbol{\mu}_{2,i}}\{\boldsymbol{w}_i^{\mathrm{T}}\boldsymbol{\mu}_{2,i}+\boldsymbol{b}^{\mathrm{T}}\boldsymbol{m}_i\} \tag{34a}$$

s.t.

$$\boldsymbol{W}_i^{\mathrm{T}}\boldsymbol{\mu}_{2,i}=\boldsymbol{M}_i^{\mathrm{T}}\boldsymbol{b} \tag{34b}$$

$$\boldsymbol{\mu}_{2,i}\geq\boldsymbol{0} \tag{34c}$$

where $\boldsymbol{\mu}_{2,i}$ is the vector of dual variables in the inner maximum problem. Thus, problem (32) is presented as:

$$\begin{cases}\min\limits_{\boldsymbol{x},\boldsymbol{M}_i,\boldsymbol{m}_i,\boldsymbol{\mu}_{1,i},\boldsymbol{\mu}_{2,i}}\left\{\boldsymbol{a}^{\mathrm{T}}\boldsymbol{x}+\max\limits_{i\in\{1,2,...,N\}}\{\boldsymbol{w}_i^{\mathrm{T}}\boldsymbol{\mu}_{2,i}+\boldsymbol{b}^{\mathrm{T}}\boldsymbol{m}_i\}\right\}\\ \text{s.t. (13b), (33), (34)}\end{cases} \tag{35}$$

Finally, problem (35) is transformed into (36), which is solved by off-the-shelf MILP solvers.

$$\min_{\boldsymbol{x},\boldsymbol{M}_i,\boldsymbol{m}_i,\boldsymbol{\mu}_{1,i},\boldsymbol{\mu}_{2,i}}\{\boldsymbol{a}^{\mathrm{T}}\boldsymbol{x}+\Theta\} \tag{36a}$$

s.t.

$$\begin{cases}\Theta\geq\boldsymbol{w}_i^{\mathrm{T}}\boldsymbol{\mu}_{2,i}+\boldsymbol{b}^{\mathrm{T}}\boldsymbol{m}_i\quad i\in\{1,2,...,N\}\\ \text{(13b), (33), (34)}\end{cases} \tag{36b}$$

where Θ is an auxiliary variable.

D. Implementation of MADR

By solving (36), we obtain the day-ahead decision variables $\boldsymbol{x}$ and affine coefficients $\boldsymbol{M}$ and $\boldsymbol{m}$. The day-ahead decision variables are implemented in the day-ahead scheduling. In the intra-day scheduling, the REG variations are obtained sequentially over time. Then, the affine coefficients are determined according to the distance in (26) between the current REG variations and the centroids of uncertainty subsets in (27).

V. Case Studies

A. System Configuration

The two-stage RO problem is tested in an IEHHS consisting of the IEEE 33-bus ADN and the 15-node DHN, which are colored in black and red in Fig. 4, respectively. The case parameters are configured in light of the scales of ADN and DHN. The matched scales of the ADN, DHN, and AEL could clearly reflect the complementary effects. The 15-node DHN comes from a real DHN in [32], which meets the heating demands of a general industrial park. The scale of IEEE 33-bus ADN matches the transmission range of 15-node DHNs. The HE is configured with a rated capacity of 0.65 MW to satisfy the maximum heat dissipation of 2 MW AEL. The electric and heat power profiles are given in Fig. 5, where P^{WT} and P^{PV} are the electric power of wind turbine (WT) and photovoltaic (PV), respectively; and P^{D} and H^{D} are the power of electric and heat loads, respectively. The AEL parameters are given in Table II [24], and the IEHHS parameters are given in Table III [33]. The solving process is fulfilled in a Windows-based computer with Intel Core i5-9500 CPU at 3.0 GHz and 20 GB of RAM by using commercial solver Gurobi. The codes are written in MATLAB and Yalmip.

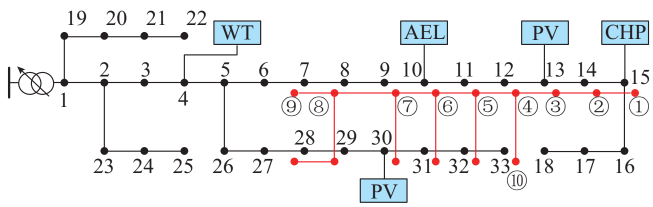

Fig. 4. Topology of IEHHS.

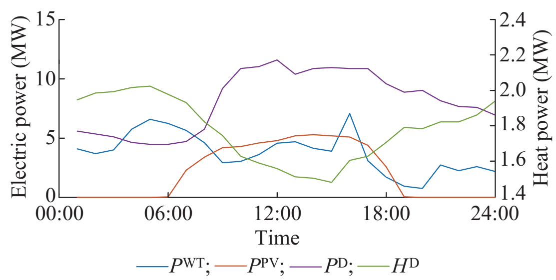

Fig. 5. Electric and heat power profiles.

TABLE II
AEL PARAMETERS

Parameter	Value	Parameter	Value
k_a	–940 W/°C	R_{EL}	0.004 °C/W
k_b	1260 W/(A·cm)	γ_{BoP}	6%
k_c	1.24×10^4 W	P^{EL}_{max}	2 MW
N_c	630	P^{EL}_{min}	0.2 MW
A_m	0.37 m^2	a_0	1 MW
u_{th}	1.48 V	T^{EL}_{max}	90 °C
C_{EL}	4.5×10^7 J/°C	T^{EL}_{min}	60 °C

TABLE III
IEHHS PARAMETERS

Parameter	Value	Parameter	Value
T_a	25 °C	C_{NG}	4.5 ¥/m^3
m^{HE}_{max}	4 kg/s	η_{CHP}	40%
H^{HE}_{max}	0.65 MW	C_w	4.2×10^3 J/(kg·°C)
H^{HE}_{min}	–0.65 MW	γ_{loss}	0.003 km^{-1}
L_{NG}	9.7 kWh/m^3	T^{s}_{max}	110 °C
V_{max}	1.21 p.u.	T^{s}_{min}	80 °C
V_{min}	0.81 p.u.	T^{r}_{max}	110 °C
C_{H2}	30 ¥/kg	T^{r}_{min}	50 °C

B. Effectiveness of BHE

In this subsection, the IEHHS operation with BHE is verified, which is compared with the unidirectional heat exchange (UHE) mode that only considers the waste heat recovery for district heating.

Figure 6 presents the AEL states in the UHE and BHE modes. In the UHE mode, the AEL keeps off in the first two hours because of the slow start-up speed. On the contrary, the AEL in the BHE mode starts up quickly using the heat from the DHN. During 09:00-11:00 and 17:00-20:00, the AEL in the BHE mode is shut down due to an insufficient REG, while the AEL in the UHE mode is in the standby state for the subsequent hydrogen production, which increases the AEL operating cost.

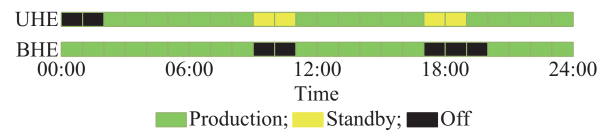

Fig. 6. AEL states in UHE and BHE modes.

Figure 7 gives the ADN scheduling results in UHE and BHE modes. There are sufficient REGs for hydrogen production during 01:00-05:00, but the AEL power P^{EL} increases slowly due to the high thermal inertia, leading to the curtailment of REGs in the start-up phase of AEL. In the BHE mode, the heat from the DHN is used to increase the temperature of AEL, and the AEL runs at the full load at 02:00. Thus, more wind power P^{WT} is utilized, and less power of CHP plants P^{CHP} is required. During 18:00-20:00, the hydrogen production is suspended due to insufficient electricity supply. In the UHE mode, the AEL keeps in the standby state, with the power consumption for the BoP. On the contrary, in the BHE mode, the AEL is shut down because of its ability to start up and shut down flexibly.

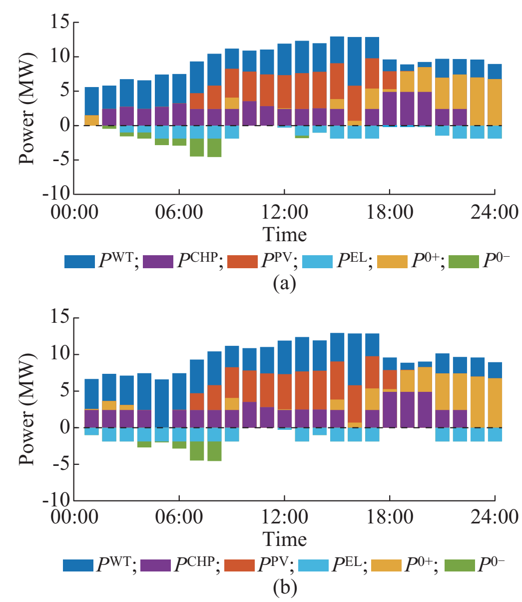

Fig. 7. AND scheduling results in UHE and BHE modes. (a) UHE mode. (b) BHE mode.

Figure 8 presents the DHN scheduling results in UHE and BHE modes, where the subscripts 1 and 2 denote the UHE and BHE modes, respectively. During 06:00-09:00, the heat from AEL is transferred to DHN to reduce the fuel cost of CHP plants. Besides, owing to the heat supplied by the AEL, the CHP plant is shut down to reduce the operating cost at 24:00. The difference between the results in UHE and BHE modes is that the exchanged heat H_2^{HE} is negative during some periods, illustrating that the AEL can be heated by DHN. In addition, more heat can be transferred to DHN in the BHE mode than that in the UHE mode, because the temperature can be adjusted quickly in the BHE mode.

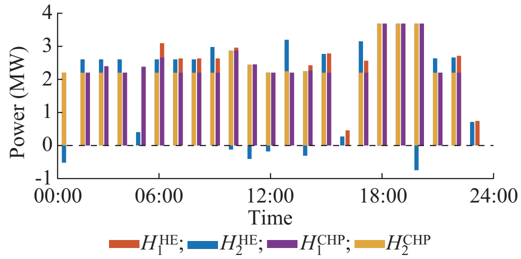

Fig. 8. DHN scheduling results in UHE and BHE modes.

Figure 9 shows the temperatures of AEL and the associated supply and return water in DHN. The heat dissipation indicates that the heat is transferred from the AEL to DHN, and the heat absorption indicates the inverse direction. The impact of BHE on the thermal dynamics of AELs is manifested as temperature changes faster. Allowing heat exchange from the DHN to AELs, AELs heat up more rapidly in the BHE mode. Based on this, the temperature drop range of AELs is expanded in the BHE mode because AELs can reach specified temperature with less time. As a result, the AEL temperature becomes lower when the heat is transmitted from AELs to DHNs, and thus BHE affects both the heating and cooling speeds of AELs. In Fig. 9, there are more AEL temperature fluctuations in the BHE mode, indicating a faster temperature adjustment speed. After the initial start-up phase, the temperature in the UHE mode ranges between 60 ℃ and 90 ℃, while the temperature in the BHE mode ranges between 30 ℃ and 90 ℃. Hence, more exhaust heat is recovered for the utilization in the BHE mode.

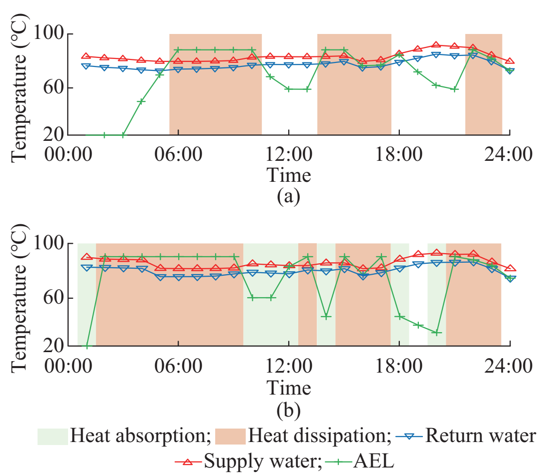

Fig. 9. Temperatures of AEL and associated supply and return water in DHN. (a) UHE mode. (b) BHE mode.

Table IV presents the IEHHS operating costs in the UHE and BHE modes. In the UHE mode, the maximum share of the CHP plant cost is taken by district heating. Simultaneously, the CHP plant generates more electricity to satisfy the electric power and heat constraints. Accordingly, the cost of purchasing electricity from upstream grids is lower in the UHE mode. In the BHE mode, more hydrogen is produced because of the enhanced flexibility. Meanwhile, more heat is recovered, which reduces the district heating costs. To sum up, the BHE mode reduces the IEHHS operating cost by about 6%.

TABLE IV
IEHHS OPERATING COST IN UHE AND BHE MODES

Mode	Cost of purchasing electricity (¥)	CHP plant cost (¥)	Revenue of selling hydrogen (¥)	IEHHS operating cost (¥)
UHE	13694	68305	16474	65524
BHE	14314	66694	19356	61652

C. Performance of Robust Scheduling with MADR

In this subsection, the performance of MADR for considering variations of REG is evaluated. The optimization results obtained by MADR and SADR are compared, and the results obtained by deterministic optimization (DO) neglecting uncertainties are given for comparison. Besides, we evaluate the impact of the number of clusters on the total net cost, reliability, and computation time using the MADR. 500 new scenarios are generated for out-of-sample tests, and the average results are given in Table V, where MADR-n denotes that there are n clusters in the MADR. Penalty costs come from purchasing electricity from upstream grids to compensate for the intra-day power deficiency. Thus, a higher penalty cost means a lower robustness of the scheduling method.

TABLE V
COMPARISON OF AVERAGE RESULTS IN 500 SCENARIOS WITH DIFFERENT METHODS

Method	Total net cost (¥)	Penalty cost (¥)	Computation time (s)
DO	97346	9803	31
SADR	88482	5283	201
MADR-2	87084	3192	296
MADR-3	85505	1397	484
MADR-4	84045	971	649
MADR-5	82909	695	931
MADR-6	82142	531	1189
MADR-7	81375	495	1424
MADR-8	80833	363	1798
MADR-9	80396	349	2219
MADR-10	79859	339	2640

According to Table V, both the total net cost and penalty cost of DO are the highest among all the methods, while the computation time is the lowest. This is because the variations of REGs are not considered in DO, resulting in the highest adjustment cost and lowest computational burden in intra-day operations. Compared with SADR, MADR provides more targeted ADRs by uncertainty set clustering, leading to a decrease in total net cost and penalty cost. Compared with DO and SADR, MADR-10 reduces the total net cost by about 17.9% and 9.7% and the penalty cost by

96.5% and 93.6%, respectively. It is demonstrated that a more fine-grained division of the uncertainty set effectively reduces the operating costs and improves robustness. However, as the number of clusters increases, the reductions in penalty cost and the total net cost gradually slow down while the computation time increases significantly. Among all the MADRs, MADR-5 achieves a balance between the total net cost and computation time. Hence, we select MADR-5 for the subsequent analyses.

The total net cost and computation time with different numbers of clusters are presented in Fig. 10. With the increasing number of clusters, the total net cost monotonically decreases, but the downtrend is slowing down. In this regard, the elbow method is a common way to determine the balance point. In Fig. 10, the elbow point is approximately at 5. The decline speed of total net cost before 5 is much faster than that after 5. Besides, the computation time also needs to be considered. The growth of computation time gets faster with the increasing number of clusters. When the number of clusters is 5, the computation time is about 1000 s, while it reaches about 1500 s when the number of clusters is 6, indicating that solving the two-stage RO problem with MADR-6 is much more time-consuming compared with MADR-5. Thus, MADR-5 strikes the best balance between cost reduction and computation time.

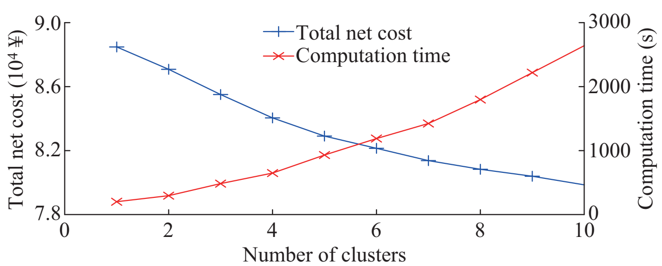

Fig. 10. Total net cost and computation time with different numbers of clusters.

Table VI gives the scales of the two-stage RO problem, where n_{RE} and n_{ADR} are the numbers of REGs and ADRs, respectively. The primal problem includes a total of 552 and 408 variables at the first and second stages. The primal problem also contains a total of 7431 linear constraints. Since the primal problem cannot be solved directly, the dual problem reflects its true computational scale. According to Table VI, as the number of ADRs increases, the numbers of variables as well as constraints increase linearly. However, due to the limitation of computational resources, the computation time increases rapidly, so there is a point where the computational cost exceeds the computational benefit. Nevertheless, the two-stage RO problem is solved at the day-ahead decision-making stage, where the computation time is considered acceptable.

The comparison of operation states obtained by DO, SADR, and MADR-5 is shown in Table VII. During 10:00-11:00, the AEL is off according to the DO solutions, and it is in the production state according to RO solutions (SADR and MADR-5 solutions). This is because the REG is larger than expected and more hydrogen would be produced if the AEL works in production states. Different from the DO solutions, the CHP plant only keeps off at 01:00 according to the RO solutions, which provides more heat for dealing with heat shortages caused by uncertainties in the intra-day operation. Compared with the SADR solution, the valve V1 obtained by MADR-5 changes more frequently, indicating that the AEL offers more flexible scheduling strategies.

TABLE VI
SCALES OF TWO-STAGE RO PROBLEM

Problem	Stage	Number of continuous variables	Number of binary variables	Number of linear constraints
Primal problem	First	552	0	3465
	Second	192	216	3966
Dual problem		$3\times 7431t_{\max}n_{\mathrm{RE}}n_{\mathrm{ADR}}$	$7431t_{\max}n_{\mathrm{RE}}n_{\mathrm{ADR}}$	$4\times 7431t_{\max}n_{\mathrm{RE}}n_{\mathrm{ADR}}$

TABLE VII
COMPARISON OF OPERATION STATES OBTAINED BY DO, SADR, AND MADR-5

Time	DO			SADR			MADR-5		
	AEL	CHP	k^{V1}	AEL	CHP	k^{V1}	AEL	CHP	k^{V1}
01:00	1	1	0	1	0	0	1	0	0
02:00	1	1	1	1	1	1	1	1	0
03:00	1	1	1	1	1	1	1	1	1
04:00	1	1	1	1	1	1	1	1	1
05:00	1	0	1	1	1	1	1	1	1
06:00	1	1	1	1	1	1	1	1	1
07:00	1	1	1	1	1	1	1	1	1
08:00	1	1	1	1	1	1	1	1	1
09:00	1	1	1	1	1	1	1	1	1
10:00	0	1	0	1	1	1	1	1	0
11:00	0	1	0	1	1	1	1	1	1
12:00	1	1	0	1	1	1	1	1	1
13:00	1	1	1	1	1	0	1	1	1
14:00	1	1	0	1	1	1	1	1	0
15:00	1	1	1	1	1	1	1	1	1
16:00	1	0	1	1	1	1	1	1	1
17:00	1	1	1	1	1	1	1	1	0
18:00	0	1	0	1	1	0	1	1	0
19:00	0	1	0	0	1	1	0	1	0
20:00	0	1	0	0	1	0	0	1	0
21:00	1	1	1	0	1	1	0	1	1
22:00	1	1	1	1	1	1	1	1	1
23:00	1	0	1	1	1	1	1	1	1
24:00	1	0	0	1	1	0	1	1	0

Figure 11 illustrates the ADRs for the utilization of REGs at noon, where α is the renewable power variation. For PV1, the slope of linear affine functions is 1 for all the clusters, which means that the power generation of PV1 is fully utilized at the intra-day operation stage. For PV2, the slope of affine functions of cluster 5 is the largest due to the slightest variation of REGs in cluster 5. For WT, the intercepts of affine functions for different clusters are similar, which indicates that the utilized power would be similar when the power variation is zero. The slope of cluster 3 is the largest because of the slightest power variation. Accordingly, more power is utilized when the power variation falls within cluster 3.

The operating costs of out-of-sample tests by DO, SADR, and MADR-5 are given in Table VIII. The SADR and MADR-5 have similar day-ahead costs. At the intra-day operation stage, the costs in the average and worst scenarios obtained by the MADR are smaller. The total net costs obtained by the MADR-5 are 4.6% and 4.9% smaller than those by the SADR in the average and worst scenarios, respectively. In addition, the standard deviation of costs obtained by MADR-5 is also smaller, indicating more reliable scheduling strategies.

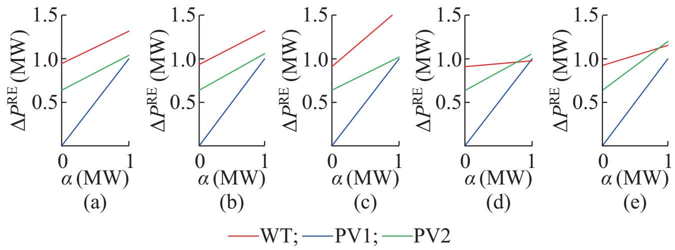

Fig. 11. Illustration of ADRs for utilization of REGs at noon. (a) Cluster 1. (b) Cluster 2. (c) Cluster 3. (d) Cluster 4. (e) Cluster 5.

TABLE VIII
OPERATING COSTS OF OUT-OF-SAMPLE TESTS BY DO, SADR, AND MADR-5

Method	Day-ahead cost (¥)	Day-ahead revenue (¥)	Intra-day cost (¥)		Intra-day revenue (¥)		Total net cost (¥)		
			Average scenario	Worst scenario	Average scenario	Worst scenario	Average scenario	Worst scenario	Standard scenario
DO	84756	19232	48570	80410	16748	27728	97346	118210	61220
SADR	106953	13523	2006	30	8512	128	86924	93332	22382
MADR-5	104865	12154	1860	765	11662	4798	82909	88678	18020

Figure 12 depicts the distribution for total net costs of scheduling strategies obtained by DO, SADR, and MADR. The operating costs of scheduling strategies obtained by the SADR and MADR are more concentrated than those obtained by the DO, indicating that the RO offers lower operational risks and costs. By comparing the MADR and SADR results, it is found that the largest cost obtained by MADR is smaller, which shows that MADR achieves higher economic efficiency. The total net costs of scheduling strategies obtained by SADR and MADR in each scenario are given in Fig. 13, where most of the points are located above the isocost line; thus, MADR reduces the operating cost in most of the scenarios.

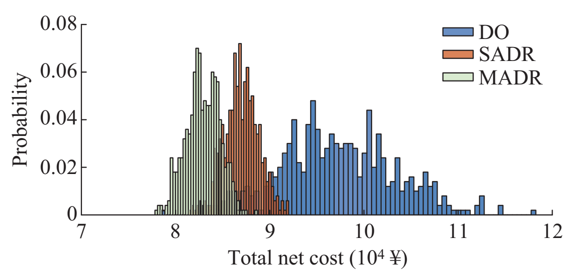

Fig. 12. Distribution for total net costs of scheduling strategies obtained by DO, SADR, and MADR.

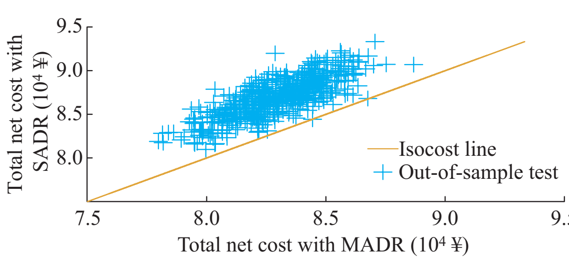

Fig. 13. Total net costs of scheduling strategies obtained by SADR and MADR.

VI. CONCLUSION

In this paper, a robust scheduling of IEHHS is proposed considering the BHE between AELs and DHNs. First, the coordinated operation model of the IEHHS consisting of AELs, ADNs, and DHNs is developed. Then, a two-stage robust problem for the scheduling of IEHHS is proposed to cope with the REG variations, and the MADR is proposed to solve the two-stage RO problem. The following conclusions are drawn.

Compared with UHE, which only considers heat exchange from AELs to DHNs, the BHE enhances the temperature adjustment speed and range of AELs, thus improving the operational flexibility of IEHHSs. The operating costs of IEHHSs with BHE are reduced by 6%, as compared with those with UHE.

Compared with traditional scheduling strategies, the MADR-based robust IEHHS scheduling provides different ADRs for different realizations of REG variations in the intra-day operation, and outperforms the traditional methods in terms of both operating costs and robustness in out-of-sample tests. The total net cost decreases as the number of clusters increases, but the computation time increases rapidly. MADR-5 is a balanced choice, and the total net costs obtained by MADR-5 are 4.6% and 4.9% lower than those by the SADR in average and worst scenarios, respectively.

This work helps to improve the energy utilization efficiency, enhance overall flexibility, and provide robust operation schedules for IEHHS operators. Given that the scheduling of IEHHSs usually involves multiple energy suppliers, future work includes extending the IEHHS model and MADRs to distributed scheduling of IEHHSs, and investigating distributed algorithms for privacy protection.

References

[1] J. Naughton, S. Riaz, M. Cantoni *et al*., "Comprehensive optimization-based techno-economic assessment of hybrid renewable electricity-hydrogen virtual power plants," *Journal of Modern Power Systems and Clean Energy*, vol. 11, no. 2, pp. 553-566, Mar. 2023.

[2] S. Anwar and X. Li, "Production of hydrogen from fossil fuel: a review," *Frontiers in Energy*, vol. 17, no. 5, pp. 585-610, Aug. 2023.

[3] H. Ma, Z. Sun, Z. Xue *et al*., "A systemic review of hydrogen supply chain in energy transition," *Frontiers in Energy*, vol. 17, no. 1, pp. 102-122, Feb. 2023.

[4] J. Chen, H. Chen, Z. Liang *et al*., "An exergy analysis model for the optimal operation of integrated heat-and-electricity-based energy systems," *Protection and Control of Modern Power Systems*, vol. 9, no. 1, pp. 1-18, Jan. 2024.

[5] Á. Serna, I. Yahyaoui, J. E. Normey-Rico *et al*., "Predictive control for hydrogen production by electrolysis in an offshore platform using renewable energies," *International Journal of Hydrogen Energy*, vol. 42, no. 17, pp. 12865-12876, Apr. 2017.

[6] H. Fan, E. Lu, W. Yu *et al*., "Multi-agent deep reinforced co-dispatch of energy and hydrogen storage in low-carbon building clusters," *IEEE Transactions on Network Science and Engineering*, vol. 11, no. 6, pp. 5449-5462, Nov. 2024.

[7] M. G. Dozein, A. M. D. Corato, and P. Mancarella, "Virtual inertia response and frequency control ancillary services from hydrogen electrolyzers," *IEEE Transactions on Power Systems*, vol. 38, no. 3, pp. 2447-2459, May 2023.

[8] J. M. Yusta and G. Matute, *Comprehensive Renewable Energy*. Amsterdam: Elsevier, 2022.

[9] G. Matute, J. M. Yusta, J. Beyza *et al*., "Multi-state techno-economic model for optimal dispatch of grid connected hydrogen electrolysis systems operating under dynamic conditions," *International Journal of Hydrogen Energy*, vol. 46, no. 2, pp. 1449-1460, Jan. 2021.

[10] C. Varela, M. Mostafa, and E. Zondervan, "Modeling alkaline water electrolysis for power-to-x applications: a scheduling approach," *International Journal of Hydrogen Energy*, vol. 46, no. 14, pp. 9303-9313, Feb. 2021.

[11] J. Li, J. Lin, Y. Song *et al*., "Operation optimization of power to hydrogen and heat (P2HH) in ADN coordinated with the district heating network," *IEEE Transactions on Sustainable Energy*, vol. 10, no. 4, pp. 1672-1683, Oct. 2019.

[12] D. Burrin, S. Roy, A. P. Roskilly *et al*., "A combined heat and green hydrogen (CHH) generator integrated with a heat network," *Energy Conversion and Management*, vol. 246, p. 114686, Oct. 2021.

[13] Q. Hu, J. Lin, Q. Zeng *et al*., "Optimal control of a hydrogen microgrid based on an experiment validated P2HH model," *IET Renewable Power Generation*, vol. 14, no. 3, pp. 364-371, Feb. 2020.

[14] C. Huang, Y. Zong, S. You *et al*., "Economic model predictive control for multi-energy system considering hydrogen-thermal-electric dynamics and waste heat recovery of MW-level alkaline electrolyzer," *Energy Conversion and Management*, vol. 265, p. 115697, Aug. 2022.

[15] Z. Wang, J. Hu, and B. Liu, "Stochastic optimal dispatching strategy of electricity-hydrogen-gas-heat integrated energy system based on improved spectral clustering method," *International Journal of Electrical Power & Energy Systems*, vol. 126, p. 106495, Mar. 2021.

[16] J. Li, J. Lin, Y. Song *et al*., "Coordinated planning of HVDCs and power-to-hydrogen supply chains for interregional renewable energy utilization," *IEEE Transactions on Sustainable Energy*, vol. 13, no. 4, pp. 1913-1929, Oct. 2022.

[17] C. Wang, Z. Gong, C. He *et al*., "Data-driven adjustable robust unit commitment of integrated electric-heat systems," *IEEE Transactions on Power Systems*, vol. 36, no. 2, pp. 1385-1398, Mar. 2021.

[18] L. Moretti, E. Martelli, and G. Manzolini, "An efficient robust optimization model for the unit commitment and dispatch of multi-energy systems and microgrids," *Applied Energy*, vol. 261, p. 113859, Mar. 2020.

[19] Y. Zhou, M. Shahidehpour, Z. Wei *et al*., "Distributionally robust unit commitment in coordinated electricity and district heating networks," *IEEE Transactions on Power Systems*, vol. 35, no. 3, pp. 2155-2166, May 2020.

[20] J. Cao, B. Yang, C. Y. Chung *et al*., "Distributionally robust management of hybrid energy station under exogenous-endogenous uncertainties and bounded rationality," *IEEE Transactions on Sustainable Energy*, vol. 15, no. 2, pp. 884-902, Apr. 2024.

[21] W. Zhao, H. Diao, P. Li *et al*., "Transactive energy-based joint optimization of energy and flexible reserve for integrated electric-heat systems," *IEEE Access*, vol. 9, pp. 14491-14503, Jan. 2021.

[22] P. Li, Z. Wu, C. Zhang *et al*., "Multi-timescale affinely adjustable robust reactive power dispatch of distribution networks integrated with high penetration of PV," *Journal of Modern Power Systems and Clean Energy*, vol. 11, no. 1, pp. 324-334, Jan. 2023.

[23] R. A. Jabr, "Linear decision rules for control of reactive power by distributed photovoltaic generators," *IEEE Transactions on Power Systems*, vol. 33, no. 2, pp. 2165-2174, Mar. 2018.

[24] Y. Zheng, S. You, H. W. Bindner *et al*., "Optimal day-ahead dispatch of an alkaline electrolyser system concerning thermal-electric properties and state-transitional dynamics," *Applied Energy*, vol. 307, p. 118091, Feb. 2022.

[25] Z. Ren, J. Wang, Z. Yu *et al*., "Experimental studies and modeling of a 250-kW alkaline water electrolyzer for hydrogen production," *Journal of Power Sources*, vol. 544, p. 231886, Oct. 2022.

[26] M. Rizwan, V. Alstad, and J. Jäschke, "Design considerations for industrial water electrolyzer plants," *International Journal of Hydrogen Energy*, vol. 46, no. 75, pp. 37120-37136, Oct. 2021.

[27] P. Olivier, C. Bourasseau, and B. Bouamama, "Dynamic and multiphysic PEM electrolysis system modelling: a bond graph approach," *International Journal of Hydrogen Energy*, vol. 42, no. 22, pp. 14872-14904, Jun. 2017.

[28] S. Chen, S. Xiang, Z. Tan *et al*., "Exploration of the oxygen transport behavior in non-precious metal catalyst-based cathode catalyst layer for proton exchange membrane fuel cells," *Frontiers in Energy*, vol. 17, no. 1, pp. 123-133, Nov. 2023.

[29] G. Pan, W. Gu, Y. Lu *et al*., "Optimal planning for electricity-hydrogen integrated energy system considering power to hydrogen and heat and seasonal storage," *IEEE Transactions on Sustainable Energy*, vol. 11, no. 4, pp. 2662-2676, Oct. 2020.

[30] A. Shabanpour-Haghighi and A. R. Seifi, "An integrated steady-state operation assessment of electrical, natural gas, and district heating networks," *IEEE Transactions on Power Systems*, vol. 31, no. 5, pp. 3636-3647, Sept. 2016.

[31] H. Qiu, Z. Li, H. Gao *et al*., "A projection and decomposition approach for multi-agent coordinated scheduling in power systems," *Journal of Modern Power Systems and Clean Energy*, vol. 12, no. 3, pp. 991-996, May 2024.

[32] X. Liu, M. Hou, S. Sun *et al*., "Multi-time scale optimal scheduling of integrated electricity and district heating systems considering thermal comfort of users: an enhanced-interval optimization method," *Energy*, vol. 254, p. 124311, Sept. 2022.

[33] C. Fu, J. Lin, Y. Song *et al*., "Optimal operation of an integrated energy system incorporated with HCNG distribution networks," *IEEE Transactions on Sustainable Energy*, vol. 11, no. 4, pp. 2141-2151, Oct. 2020.

Pengfei Han received the B.S. and M.S. degrees in electrical engineering from North China Electric Power University, Baoding, China, in 2015 and 2018, respectively. He is currently working towards the Ph.D. degree in electrical engineering in Shanghai Jiao Tong University, Shanghai, China. His research interests include optimal operation and control of integrated energy system.

Xiaoyuan Xu received the B.S. and Ph.D. degrees in electrical engineering from Shanghai Jiao Tong University, Shanghai, China, in 2010 and 2016, respectively. He was a Visiting Scholar with the Robert W. Galvin Center for Electricity Innovation, Illinois Institute of Technology, Chicago, USA, from 2017 to 2018. He is currently an Associate Professor with Shanghai Jiao Tong University. His research interests include power system uncertainty analysis and optimization.

Zheng Yan received the B.S. degree from Shanghai Jiao Tong University, Shanghai, China, in 1984, and the M.S. and Ph.D. degrees from Tsinghua University, Beijing, China, in 1987 and 1991, respectively, all in electrical engineering. He is currently a Professor with Shanghai Jiao Tong University. His current research interests include application of optimization theory to power system, electricity market, and dynamic security assessment.

Mohammad Shahidehpour received the Doctorate degree (with Hons.) in electrical engineering from the Polytechnic University of Bucharest, Bucharest, Romania, in 2009. He is also listed as a highly cited Researcher on the Web of Science (ranked in the top 1% by citations demonstrating significant influence among his peers). He is the Fellow of the American Association for the Advancement of Science (AAAS), National Academy of Inventors (NAI), Laureate of Khwarizmi International Award (KIA), and an Elected

Member of the US National Academy of Engineering. His research interests include application of optimization theory to power system, and electricity market.

Han Wang received the B.S. degree in electrical engineering from Zhejiang University, Hangzhou, China, in 2015, and the Ph.D. degree in electrical engineering from Shanghai Jiao Tong University, Shanghai, China, in 2020. From 2019 to 2020, he was a Visiting Scholar with the Robert W. Galvin Center for Electricity Innovation, Illinois Institute of Technology, Chicago, USA. He is currently an Assistant Researcher with Shanghai Jiao Tong University. His research interests include coupled operation of power-transportation network and power system uncertainty analysis.

Zhenfei Tan received the B.E. and Ph.D. degrees in electrical engineering from Tsinghua University, Beijing, China, in 2017 and 2022, respectively. He is currently a Postdoctoral Researcher with Shanghai Jiao Tong University, Shanghai, China. His research interests include electricity market, distributed resource aggregation, and non-iterative coordinated optimization.

Gang Li is the Deputy General Manager of State Grid Anhui Electric Power Co., Ltd., Hefei, China. His research interests include power grid coordinated optimization, energy storage, renewable energy, and electricity market.